Wall-modeled large-eddy simulation in a finite element framework

Herbert Owen*, Georgios Chrysokentis, Matias Avila, Daniel Mira, Guillaume Houzeaux, Ricard Borrell, Juan Carlos Cajas, Oriol Lehmkuhl

Barcelona Supercomputing Center (BSC)

Abstract

This work studies the implementation of wall modeling for large eddy simulation in a finite element context. It provides a detailed description of how the approach used by the finite volume and finite differences communities is adapted to the finite element context. The new implementation is as simple and easy to implement as the classical finite element one, but it provides vastly superior results. In the typical approach used in finite elements, the mesh does not extend all the way to the wall, and the wall stress is evaluated at the first grid point, based on the velocity at the same point. Instead, we adopt the approach commonly used in finite differences, where the mesh covers the whole domain and the wall stress is obtained at the wall grid point, with the velocity evaluated at the first grid point off the wall. The method is tested in a turbulent channel flow at $Re_\tau = 2003$, a neutral atmospheric boundary layer flow, as well as a flow over a wall-mounted hump, with significant improvement in the results compared to the standard finite element approach. Additionally, we examine the effect of evaluating the input velocity further away from the wall, as well as applying temporal filtering on the wall model input.

Keywords: Large eddy simulation, wall modeling, exchange location, law of the wall, finite elements

1. Introduction

In recent years, Large Eddy Simulation (LES) has emerged as a valuable tool for the simulation of turbulent flows at high Reynolds numbers and complex geometries, typically encountered in practical engineering applications. In this approach, the larger, dynamically important eddies are directly resolved, while the smaller ones are assumed to have a universal character and are therefore modeled. For wall-bounded flows, the cost becomes prohibitively expensive, since the dynamically important eddies in the near-wall region become smaller as the Reynolds number increases, and thus extreme mesh refinement is required to resolve them. Modeling the inner part of the boundary layer instead of resolving it alleviates this problem.

The basic principle of wall modeling is that the transport of momentum in the inner layer has to be modeled, since the grid is too coarse to resolve the dynamically important eddies near the wall and just assuming a no-slip condition results in an incorrect velocity profile and, subsequently, an incorrect stress. Several wall models, with different levels of complexity, have been developed to that effect. They can be categorized into two groups, those that directly model the wall stress and those that employ a Reynolds-averaged Navier-Stokes (RANS) approach in the inner layer. The reader can refer to [1–5] for additional information on the wall models. In this work we focus on the implementation of wall modeling for large eddy simulation in a finite element framework. The standard approach to wall modeling for LES in finite elements is the same as the one typically used in RANS, as described for example in [6–9]. As opposed to the approach commonly used in finite differences and finite volumes, the mesh does not extend all the way to the wall (i.e., a part of the domain is omitted). Therefore, there exists a thin region of height d between the wall and the first point of the computational mesh (see Fig. 1a). The traction is applied at point A with the velocity evaluated at the same point.

*Corresponding author
Email address: herbert.owen@bsc.es (Herbert Owen)

Despite its importance for simulation problems of engineering interest, little work has been conducted in regards to wall-modeled LES (WMLES) in a finite element framework. Bazilevs and Hughes [10] proposed an alternative method to deal with coarse meshes in the near-wall region, through the weak imposition of the boundary conditions using Nitsche's method [11]. The formulation was further enhanced by Bazilevs et al. in [12, 13], by incorporating the law of the wall of Spalding [14] and also imposing the boundary condition in the wall-normal direction in a weak sense, although the primary goal of the latter was ease of implementation. The weak imposition performed considerably better when uniform (and, thus, coarse) grids were utilized, as is often the case in applications of practical interest. However the results were still not very accurate. Krank and Wall [15] suggested an alternative approach to wall modeling, via the use of a function space that consists of a standard polynomial function space and an enrichment constructed on the basis of Spalding's law of the wall. This modification allows for the boundary layer to be resolved in a mean sense (somewhat resembling Detached Eddy Simulation on that respect) even with coarse meshes. Following the classification proposed in [4], the method they propose is a RANS-LES method, in contrast to the method proposed herein that classifies as a two-layer approach. The method was tested in various configurations using very coarse meshes with surprisingly accurate results.

Kawai and Larsson approached the problem from a different angle (albeit in a finite difference context) in [16]. In order to explain the mismatch between the modeled and the real skin friction that is observed when the wall stress is modeled using the nearest neighboring LES velocity (commonly referred to as Log-Layer Mismatch or LLM), they looked at the error due to the under-resolved LES in the first few grid points off the wall. They noted that there is no inherent requirement to apply a wall model at the first grid point off the wall (as is it typically done in a finite volume or finite difference context), as long as it is applied within the inner part of the boundary layer. This means that the wall model is fed with more accurate information and thus provides a better prediction of the wall shear stress, resolving the LLM problem. Instead of the typical finite difference approach, where the traction is applied on the wall with the velocity evaluated at the first grid point off the wall (points B and C respectively in Fig. 1b), they propose that the velocity is evaluated at a point further away from the wall (e.g. point D in Fig. 1b). They called this point exchange location. We will, therefore, refer to the method as the exchange location method. The typical implementation of the wall law in the finite difference community can be regarded as a particular case of the exchange location method.

Yang et al. [17] suggested that the LLM is not caused by the numerical error in the first point off the wall, as proposed in [16], but rather by the unphysically strong coupling between the wall shear stress and the velocity at the first point off the wall. They proposed an alternative solution in which the wall model receives the time-filtered LES velocity at the first point off the wall, which proved to be successful in eliminating the LLM problem. They also showed that the same effect can be achieved through the application of wall-parallel spatial filtering on the wall model input, but noted the difficulty of constructing such spatial filters in unstructured meshes. In addition, they pointed out that while the method proposed in [16] has been useful, it is impractical in complex geometry flows, imposing a large overhead on mesh generation as well as wall model implementation.

De Wiart and Murman performed WMLES in a Discontinuous Galerkin Spectral Element framework in [18]. Using a simple equilibrium wall model and high-order elements, they were able to accurately predict the turbulent channel flow even at Reynolds numbers up to $Re_\tau = 5 \times 10^5$, however the model was unable to correctly predict non-equilibrium flows such as the two-dimensional periodic hills and the NACA 4412 airfoil. In the airfoil case, they experimented with the input location for the wall model, with minimal impact on the results. Frère et al. [19] employed both the aforementioned strategies (from [16] and [17]) in the turbulent channel flow, using a high-order Discontinuous Galerkin code. They observed that applying an averaging procedure on the input of the wall model had no impact on the results. It is important to note, however, that they only applied a "partial" average (cf. Eq. 11 therein), as opposed to the full average suggested in [17]. The traction they imposed is proportional to the instantaneous velocity while the factor of proportionality depends on the average velocity. Instead, in the method proposed in [17] not only does the factor of proportionality depend on the average velocity but the traction is proportional to the average velocity. Since the method used imposes the unphysically strong coupling between the wall shear stress and the velocity of the first point off the wall, it is not expected to introduce a significant improvement according to the findings in [17]. In terms of the input location for the wall model, they found that placing the interface at the bottom of the second element off the wall, massively improved the results compared to placing it at the top of the first element. However, they did not examine locations further away from the wall. Considering the significant differences between the Discontinuous Galerkin and standard finite element methods, we believe that their conclusions are not necessarily transferable to the framework used in this article. For instance, in a continuous finite element approach the velocity is the same at the

bottom of the second element off the wall and at the top of the first element.

In the present work, we adapt the finite difference approach for wall modeling to the finite element framework and compare it with the approach typically used in the finite element community [6–9]. We also examine the exchange location method proposed in [16], as well as the application of temporal filtering on the input of the wall model, suggested in [17]. A key contribution of this work is to show that abandoning the classical finite element implementation offers significant improvements in the results.

The remainder of the paper is organized as follows. In Section 2, the strong and weak forms of the Navier-Stokes equations for incompressible flows are described, along with the numerical method used for the numerical examples presented in this paper. In Section 3, we offer a detailed description of the approach typically used in finite elements, the one commonly used in finite differences as well as the exchange location method outlined above. We specifically look at how the wall shear stress is defined in both cases and denote the differences between them. In Section 4, we present numerical results from the turbulent channel flow case at $Re_\tau = 2003$. Section 5 we present results from a neutral atmospheric boundary layer (ABL) flow over flat terrain, a case where the classical finite element approach cannot provide satisfactory results. The exchange location approach provides much better results for this case where $Re_\tau = 2.98e7$, which is representative of typical ABL flows. A more complex geometry is examined in Section 6, as we simulate the flow over a wall-mounted hump at $Re = 936000$. The separation, reattachment and recovery of the boundary layer present in this case make it an excellent benchmark case for the proposed methodology. Finally, we draw conclusions in Section 7.

2. Numerical treatment

The numerical simulations presented in this work have been performed using Alya, a high performance computing multi-physics code developed at the Barcelona Supercomputing Center [20]. Alya uses a finite element formulation to solve the incompressible Navier-Stokes equations, described below.

2.1. Incompressible Navier-Stokes problem

Let Ω be a bounded domain of $\mathbb{R}^3$, Γ its boundary and $(0, T]$ the time interval. The strong form of the incompressible Navier-Stokes problem reads:

$$\begin{aligned} \partial_t \mathbf{u} - 2\nu\nabla\cdot\varepsilon(\mathbf{u}) + \mathbf{u}\cdot\nabla\mathbf{u} + \nabla p &= \mathbf{f}, \\ \nabla\cdot\mathbf{u} &= 0 \end{aligned}$$

in $\Omega\times(0,T)$, where $\varepsilon(\mathbf{u}) = \frac{1}{2}\left(\nabla\mathbf{u} + \nabla^T\mathbf{u}\right)$ is the velocity strain rate tensor, ν is the kinematic viscosity, and $\mathbf{f}$ denotes the vector of external body forces. The problem is supplied with an initial divergence free velocity $\mathbf{u} = \mathbf{u}^0$ in Ω, $t = 0$, and boundary conditions of the form:

$$\mathbf{u} = g$$

on the Dirichlet boundary $\Gamma_D\times(0,T)$ and:

$$\sigma\cdot\mathbf{n} = \mathbf{t_n}$$

on the Neumann boundary $\Gamma_N\times(0,T)$, where $\sigma = -p\mathbf{I} + 2\nu\varepsilon(\mathbf{u})$ is the Cauchy stress tensor and $\mathbf{n}$ is the outward pointing normal. It is assumed that $\Gamma_D\cup\Gamma_N = \Gamma$ and $\Gamma_D\cap\Gamma_N = \emptyset$. The weak form of the problem consists in finding $[\mathbf{u}, p]\in L^2(0,T;\mathcal{V})\times L^1(0,T;\mathcal{Q})$ such that:

$$\begin{aligned} (\partial_t\mathbf{u},\mathbf{v}) + 2(\nu\varepsilon(\mathbf{u}),\varepsilon(\mathbf{v})) + (\mathbf{u}\cdot\nabla\mathbf{u},\mathbf{v}) - (p,\nabla\cdot\mathbf{v}) &= \langle\mathbf{f},\mathbf{v}\rangle, \\ (q,\nabla\cdot\mathbf{u}) &= 0 \end{aligned}$$

for all $[\mathbf{v}, q]\in\mathcal{V}_0\times\mathcal{Q}$, where the initial condition is satisfied in a weak sense. We define $\mathcal{V} = H^1(\Omega)$, $\mathcal{V}_0 = H^1_0(\Omega)$, $\mathcal{Q} = L^2(\Omega)/\mathbb{R}$. As usual, $L^2(\Omega)$ is the space of square-integrable functions, $H^1(\Omega)$ is a subspace of $L^2(\Omega)$ formed by functions whose derivatives also belong to $L^2(\Omega)$ and $H^1_0(\Omega)$ is a subspace of $H^1(\Omega)$ whose functions are zero on Γ.

The non-linear term has been written in its convective form, which is most commonly encountered in computational practice. In the following we consider the energy, momentum and angular momentum conserving form (EMAC) for this term, described in detail in [21]:

$$NL_{emac}(\mathbf{u}) = 2\mathbf{u} \cdot \varepsilon(\mathbf{u}) + (\nabla \cdot \mathbf{u})\,\mathbf{u} - \frac{1}{2}\nabla|\mathbf{u}|^2. \tag{1}$$

The last term of Eq. 1 was absorbed in the pressure in [21], by redefining the pressure as $p^* = p - \frac{1}{2}|\mathbf{u}|^2$, which has no physical meaning. Here, it is explicitly included in the formulation, avoiding the implementation of non-physical Neumann conditions at outflow boundaries.

The Galerkin approximation is used for space discretization. To obtain the discrete problem, the continuous spaces, $\mathcal{V}_0$ and $\mathcal{Q}$, are approximated by the discrete linear subspaces $\mathcal{V}_{0h} \subset \mathcal{V}_0$ and $\mathcal{Q}_h \subset \mathcal{Q}$. In the examples presented in this work, bilinear hexahedral elements have been used. Nevertheless, Alya can use unstructured meshes including also tetrahedra, prisms, and pyramids as well as quadratic shape functions. Temporal discretization is performed through an explicit third-order Runge-Kutta scheme, where the Courant-Friedrichs-Lewy number is set to CFL = 0.85 for all the cases presented in this work. A non-incremental fractional step method is used to stabilize the pressure. It allows for the use of finite element pairs that do not satisfy the inf-sup condition [22], such as equal order interpolation for the velocity and pressure used in this work. Therefore, mass conservation is not satisfied exactly. The perturbation to the incompressibility constraint introduces an error in the conservation of kinetic energy of $O\left(\delta t\, h^2\right)$ in the case of linear finite elements [23]. This coincides with the error obtained for finite volumes using a collocated scheme in [24, 25]. A detailed description of the numerical method used in this work together with examples for wall-resolved LES flows, that show its high accuracy and low dissipation can be found in [23]. The Vreman subgrid-scale model [26] is used for turbulence closure for all the examples presented in this work.

Taking into account that the approach we have just described is not widely used within the finite element community, we would like to mention that Alya can also use the variational multiscale (VMS) formulation [27–30] as an implicit LES model. The details of the VMS implementation available in Alya can be found in [31]. Some numerical results with this method will also be presented to show that the wall modeling approach produces significant improvements independently of the numerical treatment of the Navier-Stokes equations that is used.

3. Wall modeling

3.1. Explanation of the method

The analytical expression for the shear stress parallel to the wall at a distance $y = d$ from the wall is:

$$\overline{\tau(d)} = \overline{(\mu + \mu_{LES})\frac{\partial u_x}{\partial y}}\,\Big|_{y=d} - \rho\overline{u_x' u_y'}\,\big|_{y=d} \tag{2}$$

where x and y correspond to the streamwise and wall-normal directions respectively, while μ_{LES} refers to the turbulent viscosity introduced by the subgrid-scale model (if one is used). The first term of the RHS of Eq. 2 refers to the viscous and the modeled stress, while the second term refers to the resolved stress.

In the following, three different approaches to model Eq. 2 are presented: i) the typical approach used in finite elements, ii) the typical approach used in finite differences and iii) the exchange location method. It is worth noting at this point that an open integration rule is used in the simulations, i.e., the calculations are performed at the boundary gauss points and the corresponding exchange location points. However, we refer to grid points in the following, as if a closed (nodal) integration rule was used, in order to make an easier comparison between the finite element and finite difference approaches.

3.1.1. Classical finite element approach

The most commonly used approach for wall modeling in finite elements is to consider a mesh that does not extend all the way to the wall, as shown in Fig. 1a (see also [6–9]). In this approach, the layer between the wall and the first grid point (A) is not directly resolved. Instead it is modeled through a wall function. The velocity at point A and the

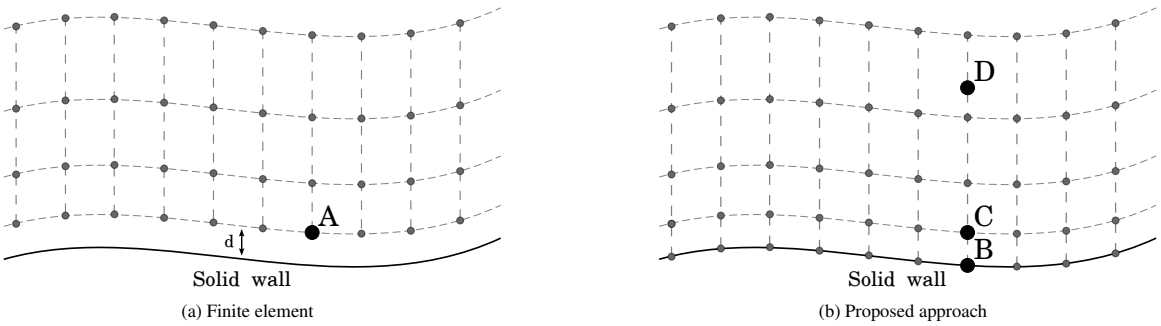

(a) Finite element (b) Proposed approach

Figure 1: Wall modeling approach in different spatial discretization methods

so-called "wall distance" between that point and the wall (denoted by d in Fig. 1a) are typically used to calculate the shear stress ($\tau(d)$), which is then imposed at point A. In addition, a no-penetration condition is imposed at that point.

This method imposes the following conditions on point A ($y = d$):

$$\overline{\tau(d)} = \overline{(\mu + \mu_{LES})\frac{\partial u_x}{\partial y}}\Bigg|_{y=d} \tag{3}$$

$$u_y = 0 \tag{4}$$

where the no-penetration condition (Eq. 4) means the resolved stress is equal to zero. Comparing Eq. 2 and 3, we see that the classical approach does not account for the effect of the resolved stress at $y = d$. Since the total shear stress is well calculated due to momentum conservation, this leads to an inaccurate prediction of the velocity gradient, i.e., the method suffers from severe Log-Layer Mismatch.

Following the classification presented in [4] for wall models, this method is essentially equivalent to a hybrid LES/RANS model, since the LES is not formally defined as extending all the way to the wall.

3.1.2. Classical finite difference approach

An alternative method proposed here involves following the approach commonly used for wall modeling in finite differences [1–5]. In this approach, the grid extends all the way to the solid wall (Fig. 1b) and we are, in fact, imposing the wall shear stress at $y = 0$, in terms of the velocity evaluated at $y = d$, where d now denotes the distance between the first grid point (B), which now coincides with the wall, and the first grid point off the wall (C). Due to the fact that this velocity has a non-zero vertical component, the problem outlined in the previous paragraph in regards to the resolved stress being zero at a distance $y = d$ from the wall is solved. It is worth noting that, since in this case we are actually resolving the near-wall part of the domain, we are indirectly imposing the following shear stress at point B:

$$\overline{\tau(d)} = \overline{(\mu + \mu_{LES})\frac{\partial u_x}{\partial y}}\Bigg|_{y=d} - \rho\overline{u'_x u'_y}\Big|_{y=d} \approx \overline{\tau(y=0)} + \overline{\frac{\partial p}{\partial x}}d \tag{5}$$

where the last approximation stems from integrating the Navier-Stokes equations in the near-wall elements.

As opposed to the classical finite element approach, this method is equivalent to a wall-stress model (again following the classification of [4]), where a wall model is solved over a layer of thickness d.

3.1.3. Exchange location

The finite difference approach provides an additional opportunity (as explained in [16]). A very typical problem of wall modeling is that, even with a perfect wall model, the results would still be inaccurate, since the LES is under-resolved in the near-wall part of the domain (e.g. at the first grid point off the wall) and thus provides inaccurate information to the wall model. There is, however, no requirement for the velocity to be evaluated at the first grid point off the wall. As mentioned earlier, the only requirement is that the velocity is evaluated at a point located within in the inner part of the boundary layer, where the wall functions are typically valid. The use of the exchange location

method allows us to place the exchange interface (i.e. the point where the LES feeds information to the wall model) further away from the wall (such as point D in Fig. 1b), where the LES is more accurately resolved and, therefore, can provide a more accurate prediction for the wall shear stress.

An issue arising with this method is that, in very complex geometries, it could happen that certain exchange location points are placed outside of the computational domain. To that end, we have developed an adaptive procedure that locates the missing points and gradually reduces the distance from the corresponding wall, until the point is located inside the computational domain. This procedure was not necessary in the cases examined in this article, however the method has been successfully used in both the realistic car model DrivAer [32] and the NASA Common Research Model (CRM) [33] . Moreover, no additional meshing effort is required in our experience.

3.2. Parallel implementation

Normally, in a parallel simulation, it is not possible to know in advance which parallel processes the exchange interface will be located in. It is also to be expected that partitions requiring information for the wall model will not host the needed exchange location points and thus communications will be necessary. To this end, a pre-process stage to construct a communication scheme is proposed in Algorithm 1. Given that all the partitions perform the same tasks, the description is done in terms of one of them.

Algorithm 1 Definition of the communication scheme for the exchange location method.

- Define the bounding box of my physical domain.
- Exchange bounding boxes with all other partitions.
- Define a bounding box containing my exchange location points and check for intersections with the bounding boxes of other parallel partitions. If there is an intersection, mark the partition as a neighbor.
- Send the coordinates of my needed points to my neighbors and receive coordinates from them.
- For each neighbor, check if their needed points are contained in my elements. Mark the contained points as 'hosted nodes'.
- Exchange the hosted nodes' list with my neighbor partitions.
- Build the communications scheme according to the 'hosted nodes' lists.

A graphical description of this procedure is shown in Fig. 2, where the bounding box of the exchange location points of partition 1 is shown together with the bounding box of partitions 2 and 3. In this example, partition 1 will receive information from partitions 2 and 3. It is important to note that this procedure is not necessary for the classical finite difference approach (i.e., when the exchange location is placed at the first grid point off the wall), which is a significant advantage in terms of the simplicity of implementing the method in a finite element code.

3.3. Wall modeling tools

Two different wall functions are utilized in the tests performed in this work, one for smooth walls and the other one for rough walls. Reichardt's extended law of the wall [34]:

$$u^+ = \frac{1}{\kappa} ln\left(1 + \kappa y^+\right) + 7.8 \cdot \left(1 - e^{-\frac{y^+}{11}} - \frac{y^+}{11} \cdot e^{-0.33 y^+}\right) \tag{6}$$

is used in the turbulent channel and wall-mounted hump cases, where u^+ and y^+ denote the dimensionless velocity and wall distance respectively, and $\kappa = 0.41$ is the von Kárman constant. Ideally, a single wall model would be utilized in all the cases presented, in order to avoid adding an extra degree of freedom in the assessment of the method. However, due to the roughness of the wall in the atmospheric boundary layer case, we use the logarithmic law for rough walls and neutral stability:

$$u_x(y) = \frac{u_*}{\kappa} ln\left(\frac{y + y_0}{y_0}\right) \tag{7}$$

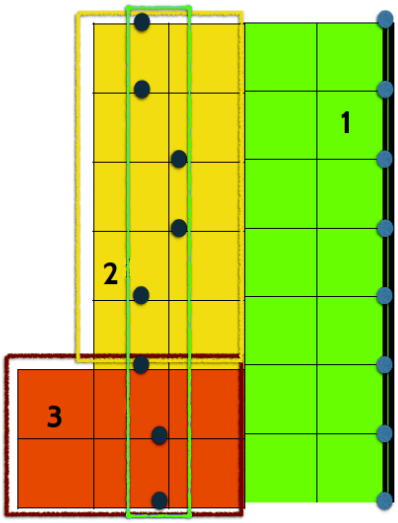

Figure 2: Neighboring subdomains containing the exchange location points

commonly used in environmental simulations. Here $u_x(y)$ denotes the mean wind speed at height y, u_* is the friction velocity, and y_0 denotes the surface roughness.

In addition, an exponential running average similar to the one proposed by Meneveau et al [35] is used to account for the time-average nature of the wall functions utilized. For any quantity ϕ, the local time average $\overline{\phi}$ at any time t_n is defined as:

$$\overline{\phi}^n = \epsilon\phi^n + (1-\epsilon)\overline{\phi}^{n-1}$$

The weighting parameter ϵ is defined as:

$$\epsilon = \frac{\delta t}{T}$$

where δt is the computational time-step and T is the characteristic averaging time-scale, chosen to be comparable to the convective time scale of the problem. In this method, the time-averaging is applied to the velocity that is used as the input for the wall model, in a similar fashion to [17]. We have confirmed in our numerical experiments that the process is insensitive to the precise value of T, as pointed out by Yang et al. in [17], provided that it is large enough (not shown here).

4. Turbulent channel flow

4.1. Problem definition

To assess the performance of our method, we investigate a turbulent channel flow at $Re_\tau = 2003$ with a setup similar to the one used in [13], where Re_τ is the friction Reynolds number based on the friction velocity and channel half width. We compare the two variations of the exchange location with the classical FE approach, using the DNS results of [36] as reference data.

The size of the computational domain considered herein is $6\pi\delta \times 2\delta \times 2\pi\delta$ in the streamwise, wall-normal and spanwise directions respectively, where δ is the channel half-width. The geometry of the domain is presented in Fig. 3. The streamwise and spanwise directions are assumed to be homogeneous, and thus periodic boundary conditions are applied, while a no penetration condition is imposed on the wall boundaries.

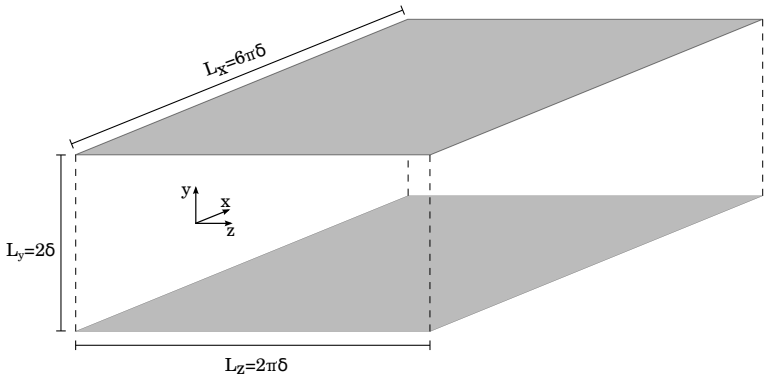

Figure 3: Computational domain for the turbulent channel case

Meshes of 64^3 (G1), $128x96x96$ (G2) and $256x128x128$ (G3) linear elements that are uniform in all directions are employed. That results in $y^+ \approx 63$, $y^+ \approx 42$ and $y^+ \approx 31$ respectively at the first node. The reference DNS used a $6144 \times 633 \times 4608$ mesh on a domain with size $8\pi \times 2 \times 3\pi$ in the streamwise, wall-normal and spanwise directions respectively. The flow is driven by a constant pressure gradient in the streamwise direction.

The simulation is run for an appropriately long time to guarantee that a statistically stationary regime is reached. Once that quasi-steady state has been achieved, statistics are collected, and the results are averaged in time for approximately 24 flow-through units (we define a flow-through unit as $t = L_x/U$ where U denotes the velocity at the center of the channel and L_x is the size of the domain in the streamwise direction). They are subsequently averaged in space (in the streamwise and spanwise direction) and non-dimensionalized using the computed friction velocity (the same applies to all the cases presented in this work). Reichardt's extended law of the wall (Eq. 6) is used for modeling the wall layer. The averaging period T is equal to two flow-through units.

4.2. Numerical results

Three alternatives for applying the wall law are compared. In the first one, which will be labeled "classical" approach in the following, we employ the standard FE approach to wall modeling, as described in Section 3. The wall distance is set equal to the height of the elements ($d = h_{el}$). The remaining two make use of the exchange location method described in this paper (cf. Section 3) at two different locations: one on the first grid point off the wall and the other at a distance of $y = 0.125\delta$. The second location is intentionally chosen to be at the limit of the wall law's validity, to evaluate the approach proposed in [16]. We note here that it is not necessary for the exchange location to coincide with the grid points. Additionally, we evaluate the effect of using temporal averaging on the input velocity of the wall law (as described in Section 3.3), by performing the two exchange location simulations with and without averaging.

Results for the mean streamwise velocity are presented in Fig. 4a, for grid G1. It becomes immediately obvious that the classical FE approach cannot accurately predict the flow, resulting in a vast overprediction of the mean streamwise velocity. Specifically, the velocity at the first grid point is in agreement with the DNS data (as expected, since that is the point where the wall law is applied), however the velocity gradient is inaccurately predicted in the first few near-wall elements resulting in a significant error in the mean streamwise velocity as we approach the core of the channel. This overprediction is a result of omitting the resolved part of the stress as explained in Section 3.1.1, leading to a severe Log-Layer Mismatch. The results from the classical FE approach are similar to the ones in [13]. When the exchange location is used, however, the prediction for the mean flow is significantly more accurate. Placing the exchange location further away from the wall offers a slight improvement in the results. However, both exchange location simulations fail to accurately capture the shape of the DNS results. Additionally, it is interesting to note that the use of temporal filtering has minimal impact on the results.

The differences between methods are smaller when looking at the fluctuations, but still noticeable (Fig. 4b - 4d). All simulations overpredict the fluctuations in the streamwise direction in the near-wall region while underpredicting

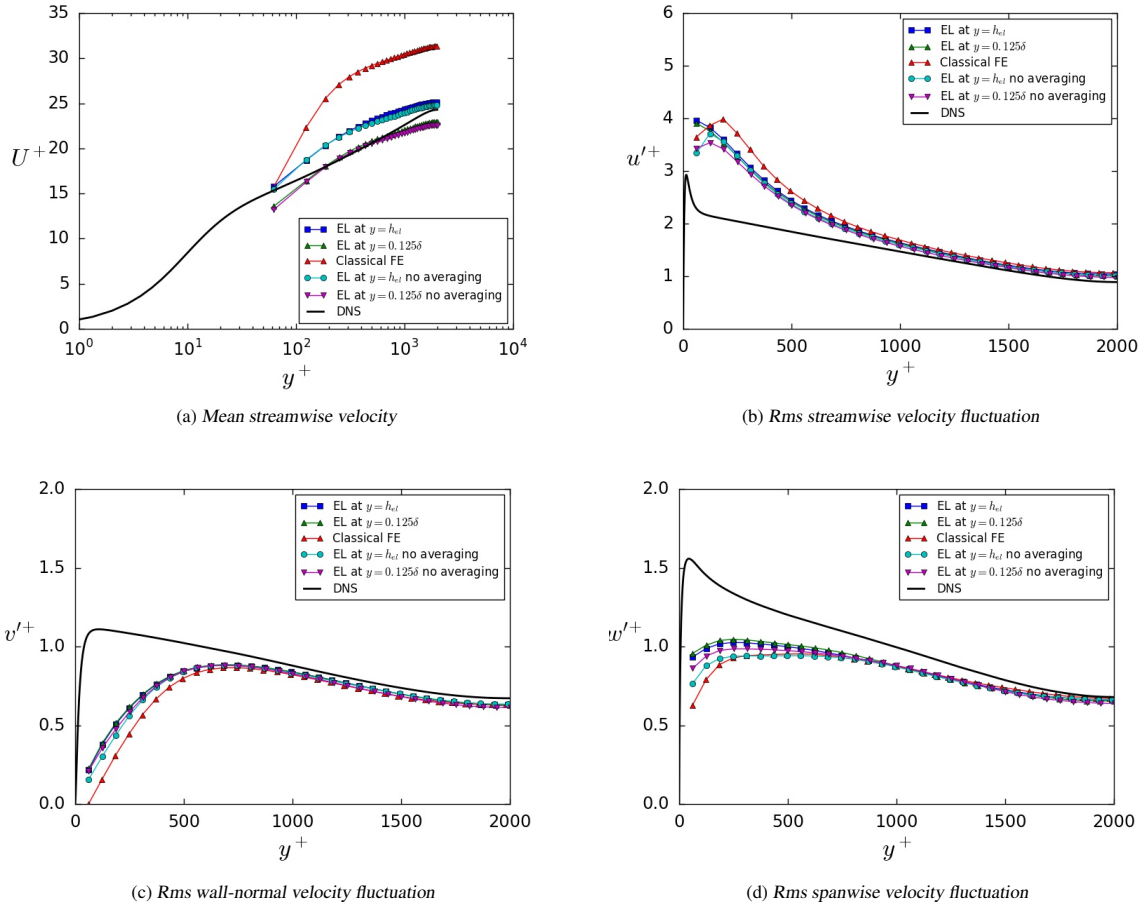

(a) *Mean streamwise velocity*

(b) *Rms streamwise velocity fluctuation*

(c) *Rms wall-normal velocity fluctuation*

(d) *Rms spanwise velocity fluctuation*

Figure 4: Mean streamwise velocity and rms velocity fluctuations, for grid G1

the wall-normal and spanwise fluctuations. The predictions are much more accurate as we approach the core of the channel. This behavior is expected since the wall law only accounts for the mean velocity profile and the coarse mesh employed does not allow for the near-wall part of the fluctuations to be accurately resolved. Another possible cause is the use of linear elements since they typically falter in accurately predicting the fluctuations near the wall (cf. [28]). That said, the exchange location method still offers an improvement in results, especially near the wall. We also have to note the fact that $v' = 0$ at $y \neq 0$ for the classical implementation of the wall law in the finite element context, which is an inherent problem of the method.

Fig. 5 presents the influence of grid refinement on the mean streamwise velocity, when the exchange location method with temporal averaging is used. It is clear that refining the grid offers a significant improvement in the results, with the prediction for grid G3 (top) being very close to the DNS results, especially when the exchange location is placed at $y = 0.125\delta$. Simulations using the classical FE method were also performed for grids G2 and G3, with similar trends to those of grid G1 (not shown here). The effect of placing the exchange location at the 4th grid point was also examined, however the results were identical to those with the exchange location at $y = 0.125\delta$.

We would like to emphasize the superior performance of the exchange location compared to the classical FE approach. Even when the exchange location is considered at the first grid point off the wall (which is essentially the standard finite difference approach adapted to finite elements), the improvement in results over the classical FE approach is astounding. It is interesting to note that despite the equivalence between finite elements and finite differences when structured grids and a closed integrating rule are used (cf. [37]), the approach when it comes to wall modeling

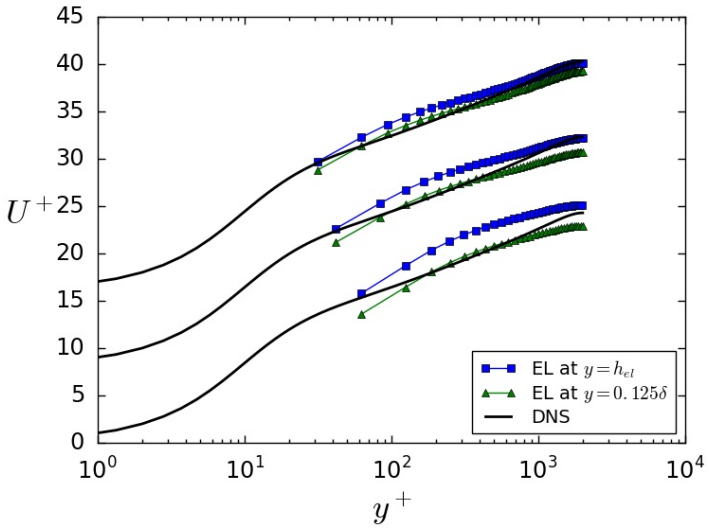

Figure 5: Mean streamwise velocity for grids G1 (bottom), G2 (middle) and G3 (top), each shifted upward by 8 units for clarity

is radically different. In this work, we demonstrate that the finite difference approach is significantly more accurate. We believe this to be an important result, especially given the simplicity of the method and its implementation in a finite element code.

Apart from the results presented here, where the formulation stabilizes only the pressure and an explicit subrid-scale model is used for turbulence closure, the method was also tested with a variational multiscale (VMS) formulation using algebraic subscales (cf. [27–30]), where no turbulent model is used (i.e., no eddy viscosity is present). As shown in Figure 6, similar conclusions can be drawn, with the difference between the classical FE method and the exchange location method being even higher.

5. Atmospheric boundary layer

5.1. Problem definition

A large scale environmental flow, namely the neutral atmospheric boundary layer flow over a flat terrain is considered in this section. The very high Reynolds number of environmental flows (here, $Re_\tau = 2.98e7$) makes the use of wall modeling imperative and the coarse resolutions used provide an excellent test for the assessment of wall modeling approaches. The size of the computational domain examined herein is $L_y = H = 1000$ m in the vertical direction and $L_x = L_z = 2\pi L_y$ in the tangential directions. The computational grid consists of 53 uniform elements in each direction. Periodic boundary conditions are imposed in the tangential directions. A stress-free condition is imposed at the upper boundary, while a no-penetration condition is imposed at the bottom and top boundaries. The logarithmic law (Eq. 7) is used to model the wall layer at the bottom boundary. The values chosen for the friction velocity and roughness length are $u_* = 0.45$ m s^{-1} and $y_0 = 0.1$ m respectively. Statistics are collected once the quasi-steady state has been achieved, and the results are averaged in time for approximately 50 flow-through units (here we define a flow-through unit as $t = U_{top}/L_x$, where U_{top} is the velocity at the top of the domain and L_x is the size of the domain in the streamwise direction), and subsequently in space (in the streamwise and spanwise direction). The averaging period T is set equal to one flow-through unit.

5.2. Numerical results

Fig. 7 presents the results for the mean streamwise velocity compared with the theoretical values from the log-law. As observed, both the exchange location simulations offer more accurate predictions than the one using the classical

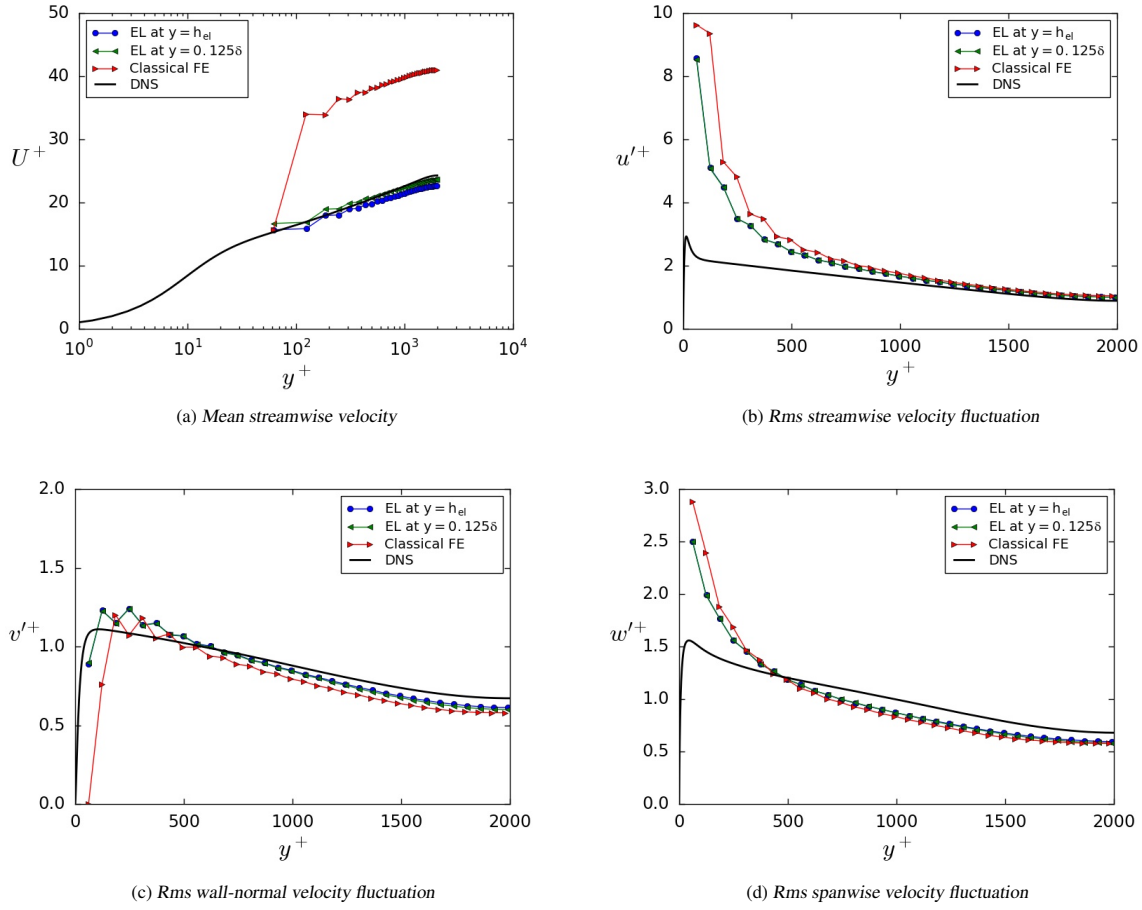

(a) *Mean streamwise velocity*

(b) *Rms streamwise velocity fluctuation*

(c) *Rms wall-normal velocity fluctuation*

(d) *Rms spanwise velocity fluctuation*

Figure 6: Mean streamwise velocity and rms velocity fluctuations, for grid G1 using a VMS formulation

FE method. Especially the results from the exchange location at the third point are very similar to the theoretical values, albeit with a slight underprediction at the part between the wall and the exchange location.

Another quantity of interest in the study of environmental flows is the non-dimensional vertical gradient of the mean streamwise velocity, defined as $\Phi = (\kappa y/u_*)(dU/dy)$. It can be seen in Fig. 8 that all simulations deviate from the theoretical value of 1 in the near-wall region. Nevertheless, the results are noticeably better for the simulations using the exchange location method, with the error being significantly higher in the near-wall region when using the classical FE method.

6. Wall-mounted hump

6.1. Problem definition

In this section, we consider the flow over a wall-mounted hump. The features of this flow, where separation, reattachment and recovery of the boundary layer occur, are of special interest, as they appear in several industrial applications. The configuration of the flow is based on the one presented by Park in [38], and the results are compared with the experimental data of Greenblatt et al. [39]. The size of the computational domain is $4.64c$, $0.909c$ and $0.3c$ in the streamwise (x), normal (y) and spanwise (z) directions respectively, where c is the chord length of the hump. The inlet and outlet planes lie at $x/c = -2.14$ and $x/c = 2.5$ respectively with the leading edge of the hump at $x/c = 0$.

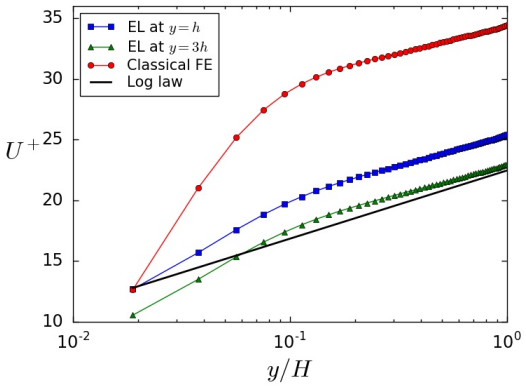

Figure 7: Mean streamwise velocity

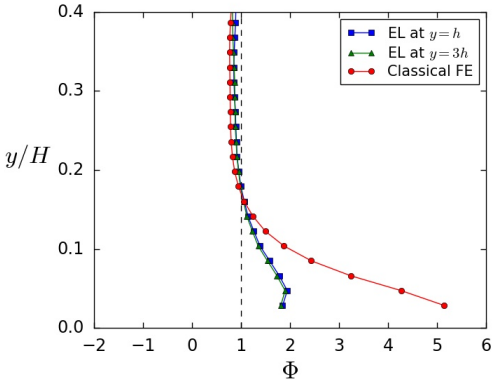

Figure 8: Non-dimensional gradient of the mean streamwise velocity, $\Phi = \left(\frac{\kappa y}{u_*}\right)\left(\frac{dU}{dy}\right)$

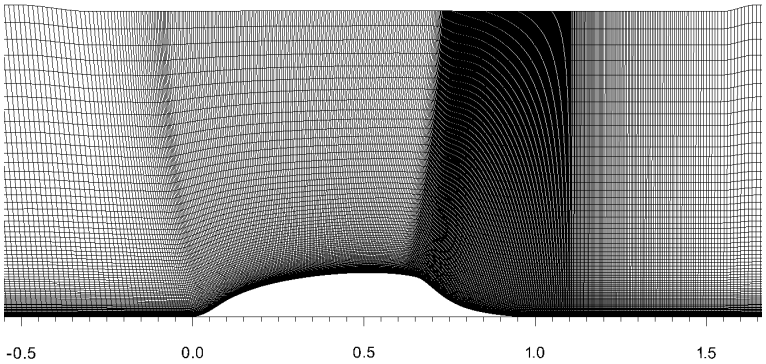

Figure 9: Computational mesh from grid G1 in the vicinity of the hump

The top wall is contoured with a small constriction (see Fig. 9) between $x = -0.5$ and $x = 1.5$ to account for the presence of the side-plates in the experiments, following the guidelines of the NASA CFDVAL2004 workshop.

The Reynolds number of the flow is $Re = 936000$, based on the hump chord length c and the free stream velocity U_∞ at the inlet. A slip boundary condition is imposed at the top boundary, while periodicity is used in the spanwise direction. A no-penetration condition is imposed at the bottom boundary, with the wall stress being fed into the simulation through the wall model (Reichardt's extended wall law is used, Eq. 6). The averaging period is set to $T = 10c/U_\infty$.

Two different grids are utilized in the simulations. The coarse grid (G1) consists of approximately 3.1 million linear elements, with $743x71x61$ nodes in the streamwise, normal and spanwise directions respectively. In the fine grid (G2) significant refinement was performed in the tangential directions. In the wall-normal direction, the first grid point was kept at the same distance from the wall (thus y^+ remained the same), so that it remains outside of the buffer layer, however the node density was increased, resulting in a reduction of the growth rate (from 1.06 for the coarse mesh, to 1.03). This resulted in approximately 8 million linear elements, with $901x111x81$ nodes in the streamwise, normal and spanwise directions respectively. Fig. 9 presents the mesh in the vicinity of the hump for grid G1, and the dimensionless grid spacings at the wall can be seen for both grids in Fig. 10.

Turbulent inflow data are synthesized through the use of the digital filtering technique described by Kempf et al. in [40]. Due to the limited experimental data at the inflow plane, the missing Reynolds stresses were specified to match those used by Park in [38] (left panels of Fig. 11). To ensure that realistic turbulence evolves before the flow

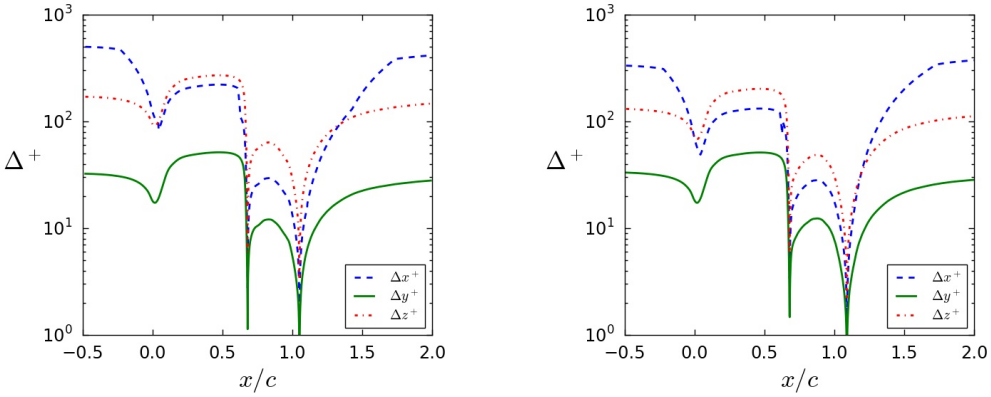

(a) *Coarse grid (G1)* (b) *Fine grid (G2)*

Figure 10: Grid spacings in wall units for the two grids.

reaches the hump, the mean velocity and Reynolds stresses from the present simulations are compared to those from the WMLES of Avdis et al. [41], at a downstream location ($x/c = -0.81$), shown in the right panels of Fig. 11, for grid G2. A slight overprediction can be observed for the streamwise Reynolds stress, which is consistent with the results presented in the turbulent channel flow in Section 4. However, the general agreement is acceptable.

Statistics are collected over approximately 20 c/U_∞ units of time, after the quasi-static state has been reached. The results are subsequently averaged in the spanwise direction.

6.2. Numerical results

Three different exchange locations are examined for this case. Aside from the exchange location at the first and third grid point off the wall, we also examine placing the exchange location at a higher point of the inner layer, without reference to the LES grid, as suggested in [4] and [16]. To that end, we choose $y = 0.125\delta_{in}$, where δ_{in} is the boundary layer thickness at the inflow plane.

The predictions for the skin friction and pressure coefficients with grid G2 are presented in Fig. 12a and Fig. 12b respectively. The results indicate that the exchange location method predicts the behavior of the flow more accurately than the classical FE method. The improvement in the prediction of the skin friction coefficient is remarkable, especially in the case of the exchange location at $y = 0.125\delta_{in}$, where the prediction for the skin friction prior to the separation is essentially identical to that of the experiments. A discrepancy is observed within the recirculation region. However, that is to be expected since a simple equilibrium model has been used. The separation and reattachment points are more accurately predicted when the exchange location method is used (cf. Table 1) for both grids. A significant improvement in the position of the reattachment point is obtained when the mesh is refined. Once more, the best results are obtained in the case of the exchange location at $y = 0.125\delta_{in}$. In terms of the pressure coefficient, all the simulations offer similar predictions. A slight underprediction is observed on the attached part of the hump when the exchange location is placed at $y = 0.125\delta_{in}$, however the shape of the "plateau" observed in the experiments around $x/c \approx 0.7 - 0.9$ is more accurately predicted.

The mean streamwise velocity profiles, obtained with the fine grid (G2), are presented in Fig. 13a at different streamwise positions. All methods capture the mean streamwise velocity profiles acceptably, even though a simple equilibrium wall model has been used. The results from the classical FE method show the highest deviation from the experiment inside the recirculation region. Due to the underprediction of the wall shear stress prior to the separation (Fig. 12a), the boundary layer carries too high momentum, resulting in early reattachment and, thus, an overprediction of the velocity profiles downstream of the reattachment point.

Fig. 13b-13d present the Reynolds stress profiles at the same streamwise positions. We observe that all simulations struggle to accurately predict the Reynolds stresses within the recirculation zone, with the predictions improving downstream of the reattachment point. The discrepancies with respect to the experimental results are similar to those

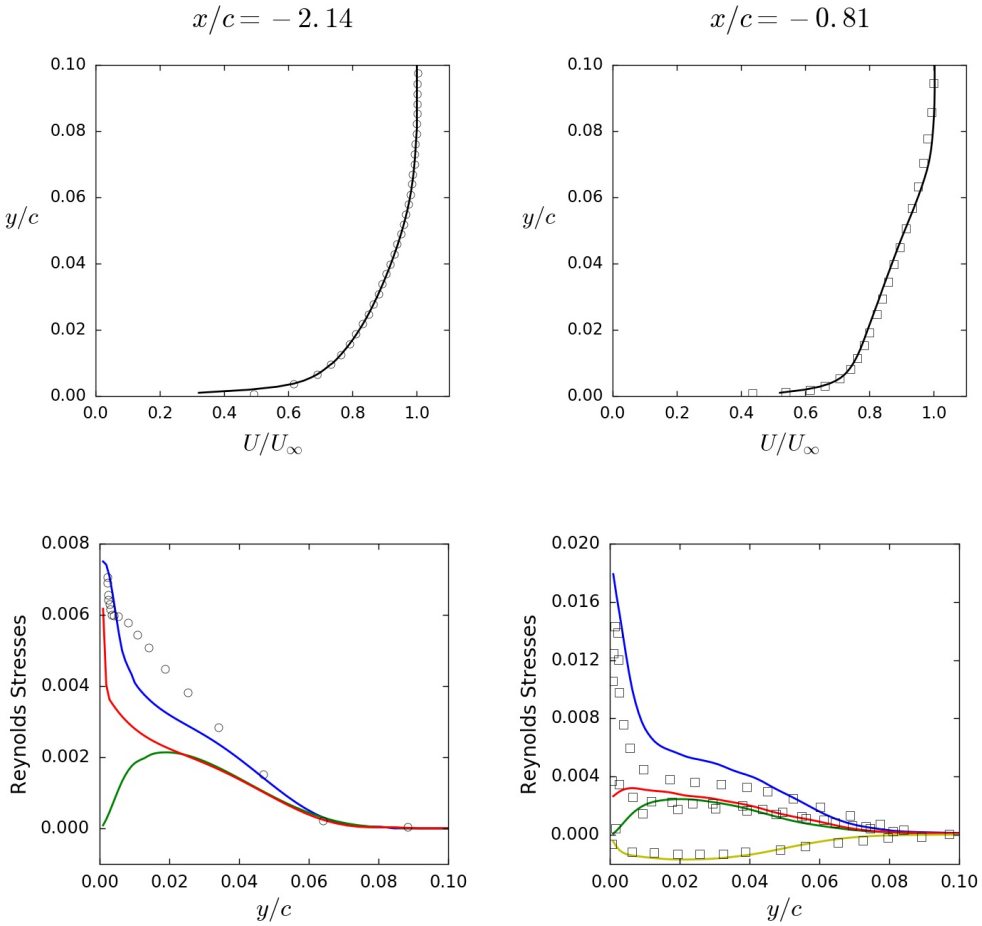

Figure 11: Mean streamwise velocity (black lines) and Reynolds stress at the inflow ($x/c = -2.14$) and a downstream location ($x/c = -0.81$), for grid G2. Blue lines: $u'u'$, green lines: $v'v'$, red lines: $w'w'$, yellow lines: $u'v'$, circles: experiment (Greenblatt et al. [39]), squares: WMLES (Avdis et al. [41]).

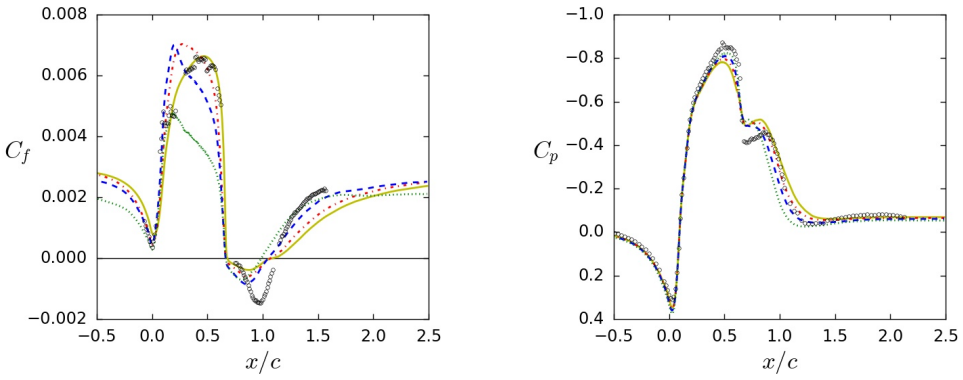

(a) *Skin friction coefficient*

(b) *Pressure coefficient*

Figure 12: Influence of the point where the velocity is evaluated on the skin friction (a) and pressure (b) coefficients across the streamwise direction (grid G2). Green dotted line: classical FE method, blue dashed line: exchange location at first grid point, red dash-dotted line: exchange location at third grid point, yellow solid line: exchange location at $y = 0.125\delta_{in}$, circles: experiment (Greenblatt et al [39]).

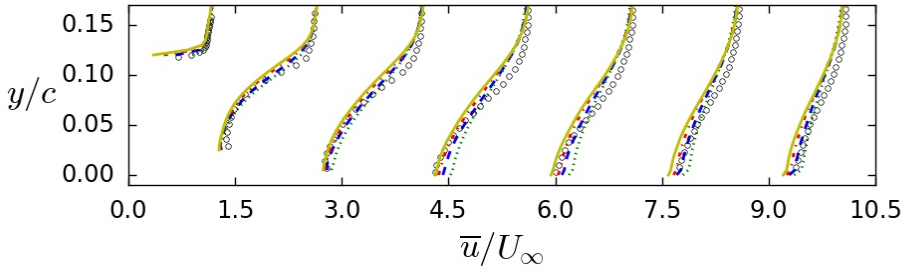

(a) *Mean streamwise velocity profiles shifted by* $\Delta = 1.5$

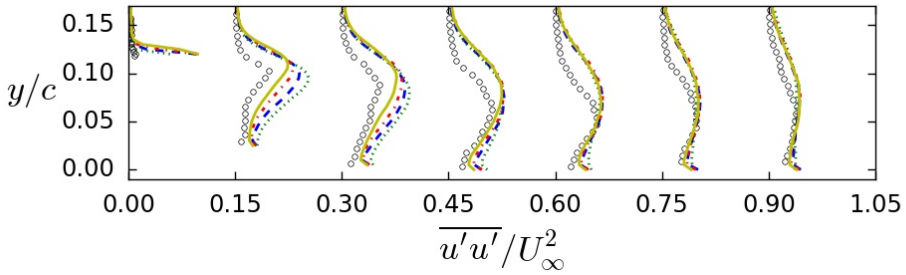

(b) *Streamwise Reynolds stress profiles shifted by* $\Delta = 0.15$

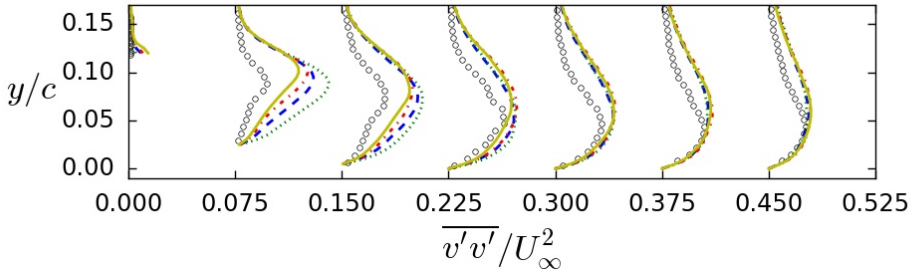

(c) *Wall-normal Reynolds stress profiles shifted by* $\Delta = 0.075$

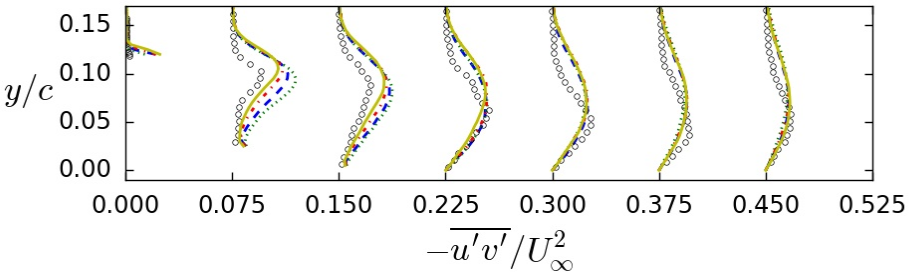

(d) *Shear Reynolds stress profiles shifted by* $\Delta = 0.075$

Figure 13: Influence of the point where the velocity is evaluated on the mean streamwise velocity and Reynolds stresses (grid G2), at different streamwise positions: $x/c = 0.65, 0.8, 0.9, 1.0, 1.1, 1.2, 1.3$. Green dotted line: classical FE method, blue dashed line: exchange location at first grid point, red dash-dotted line: exchange location at third grid point, yellow solid line: exchange location at $y = 0.125\delta_{in}$, circles: experiment (Greenblatt et al. [39]).

Simulation	x_{sep}/c G1	x_{reatt}/c G1	$(x_{reatt})_{error}$ G1	x_{sep}/c G2	x_{reatt}/c G2	$(x_{reatt})_{error}$ G2
Classical FE	0.665	0.97	11.8%	0.665	0.985	10.5%
EL at 1st point	0.665	0.99	10.0%	0.665	1.05	4.5%
EL at 3rd point	0.665	1.03	6.3%	0.665	1.07	2.7%
EL at $h = 0.125\delta_{in}$	0.67	1.05	4.5%	0.67	1.09	0.9%
Experiment	~ 0.665	~ 1.1	-			

Table 1: Separation (x_{sep}) and reattachment (x_{reatt}) locations for the different configurations

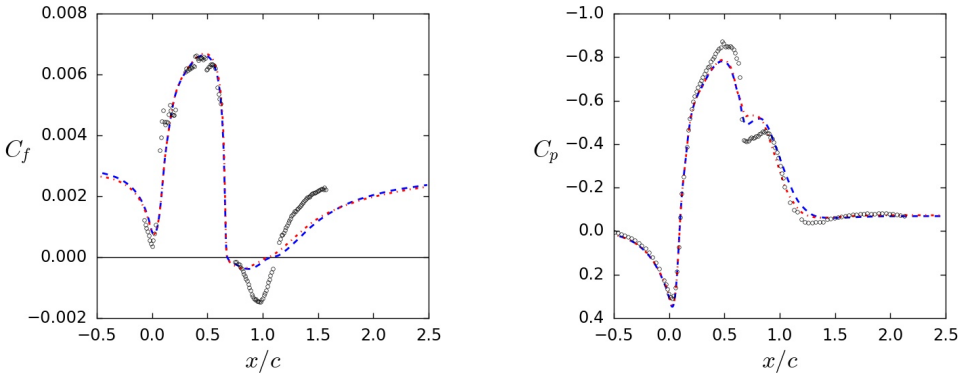

(a) *Skin friction coefficient*

(b) *Pressure coefficient*

Figure 14: Influence of grid resolution on the skin friction (a) and pressure (b) coefficients across the streamwise direction (velocity evaluated at $y = 0.125\delta_{in}$). Red dash-dotted line: coarse grid (G1), blue dashed line: fine grid (G2), circles: experiment (Greenblatt et al [39]).

observed in [38]. There exists, however a marked improvement when placing the exchange location further away from the wall.

The influence of the grid resolution on the results is presented in Fig. 14-15, for the simulations where the velocity is evaluated at $y = 0.125\delta_{in}$. Although the differences in the skin friction and pressure coefficient are hardly noticeable at first glance (Fig. 14), it can be seen that refining the mesh improves the prediction of the reattachment location (Table 1). Minimal differences are also observed for the mean streamwise velocity (Fig. 15a); however there is a significant improvement in the prediction of the Reynolds stresses close to the center of the recirculation region (Fig. 15b-15d) as the mesh is refined.

7. Conclusions

The implementation of wall modeling used by the finite difference and finite volume communities is adapted to finite elements. The new implementation is as simple and easy to implement as the classical finite element implementation but it provides vastly superior results. Instead of omitting a part of the domain and relying on the wall model to account for it, as is commonly done in finite elements, the whole domain is resolved and the wall stress at the wall is calculated using the velocity at the first grid point off the wall (or gauss point in the finite element context). The fact that this velocity is fully three-dimensional (as opposed to the classical finite element approach where the velocity used is imposed to be zero in the wall-normal direction) leads to significantly improved predictions. Specifically, the presence of the resolved part of the stress $-\rho u_x' u_z'$ (cf. Eq. 2) leads to a significantly more accurate prediction for the velocity gradient, compared to the classical finite element method. The method is tested against the classical approach, in three different benchmark cases: a) the turbulent channel flow at $Re_\tau = 2003$, b) the atmospheric boundary layer flow, and c) the wall-mounted hump flow. In all cases, the improvement in the results is significant when using the new method, in particular for the mean streamwise velocity as well as the skin friction. It is interesting to note that the proposed method performs remarkably well, despite the fact that the meshes utilized were coarse, and a simple wall law was used as a wall model. This is especially true in the hump case, a non-equilibrium flow with features like separation and reattachment of the boundary layer that are typically difficult to capture.

Additionally, two possible remedies for the LLM have been tested. Taking the input velocity for the wall law further away from the wall and using the time averaged values of the velocity. For the atmospheric boundary layer flow, due to the very high Reynolds number, time averaging is needed not only to reduce the LLM but also to avoid divergence of the simulation due to the strong fluctuations. In the channel case, we have tested the effect of time averaging the input velocity of the wall model, as well as the effect of the point where this velocity is evaluated. In this work, we do not find a significant improvement by using time-averaged velocities as an input to the wall law. The advantage of using the exchange location approach over the classical finite difference approach is also subtle for this case. It is clear that both approaches are significantly better that the classical finite element approach based on the results obtained in this work and those available in the literature. In the atmospheric boundary layer and wall-mounted hump cases, time-averaged values have been used and only the influence of the point where we evaluate the input velocity for the wall model is examined. For these two cases it is clear that the classical finite element approach provides much poorer results than the finite difference approach for wall modeling. The exchange location provides the best results for both cases. In the hump case, we observe that taking the velocity further away from the wall provides noticeable improvements for the friction coefficient and the location of reattachment point.

Acknowledgements

This work was supported by the Energy oriented Centre of Excellence II (EoCoE-II), grant agreement number 824158, funded within the Horizon2020 framework of the European Union. We would also like to acknowledge PRACE for awarding us access to the following resources: GCS Supercomputer SuperMUC at Leibniz Supercomputing Centre (www.lrz.de), Marconi at CINECA (http://www.hpc.cineca.it/) and TGCC Curie at CEA-GENCI (http://www-hpc.cea.fr). The authors thankfully acknowledges the computer resources at MareNostrum and the technical support provided by Barcelona Supercomputing Center (RES-AECT-2018-3-0028).

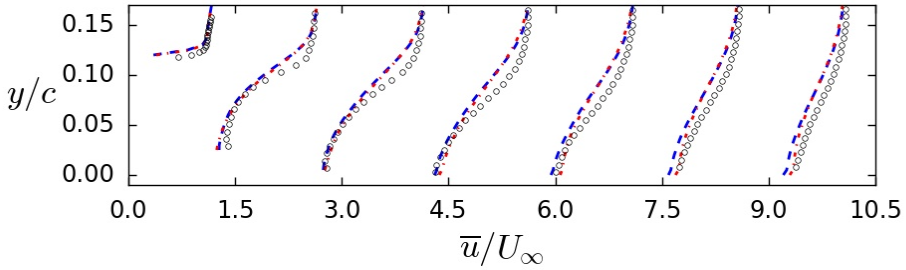

(a) *Mean streamwise velocity profiles shifted by* $\Delta = 1.5$

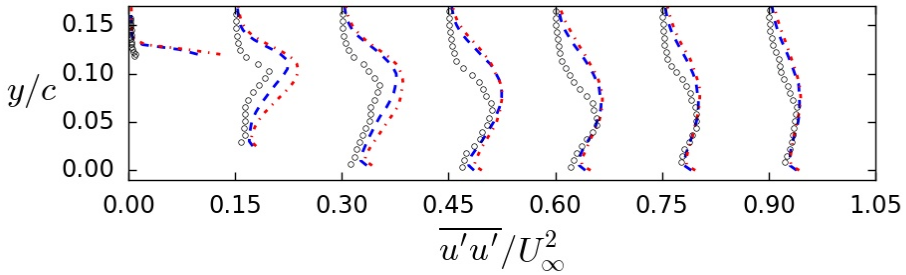

(b) *Streamwise Reynolds stress profiles shifted by* $\Delta = 0.15$

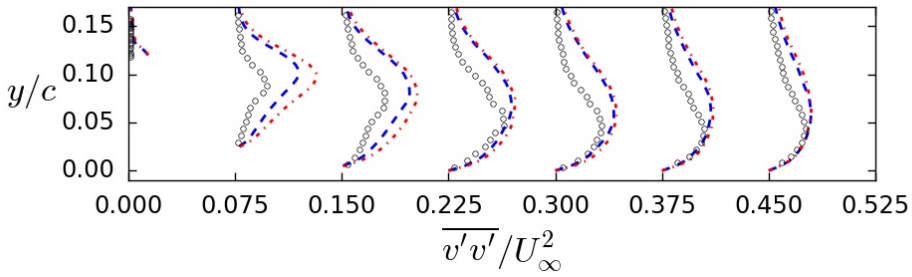

(c) *Wall-normal Reynolds stress profiles shifted by* $\Delta = 0.075$

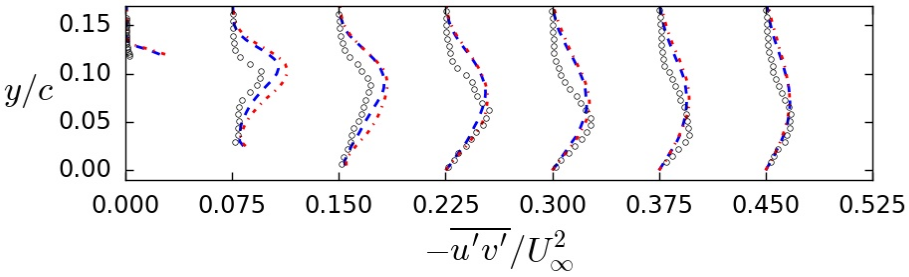

(d) *Shear Reynolds stress profiles shifted by* $\Delta = 0.075$

Figure 15: Influence of grid resolution on the mean streamwise velocity and Reynolds stresses (velocity evaluated at $y = 0.125\delta_{in}$), at different streamwise positions: $x/c = 0.65, 0.8, 0.9, 1.0, 1.1, 1.2, 1.3$. Red dash-dotted line: coarse grid (G1), blue dashed line: fine grid (G2), circles: experiment (Greenblatt et al [39]).

References

[1] P. Sagaut. *Large eddy simulation for incompressible flows - An introduction*. Springer, 3 edition, 2006.

[2] U. Piomelli and E. Balaras. Wall-layer models for large-eddy simulations. *Annu. Rev. Fluid Mech.*, 34:349–374, 2002.

[3] U. Piomelli. Wall-layer models for large-eddy simulations. *Prog. Aerosp. Sci.*, 44(6):437–446, 2008.

[4] J. Larsson, S. Kawai, J. Bodart, and I. Bermejo-Moreno. Large eddy simulation with modelled wall stress: recent progress and future directions. *Mech. Eng. Rev.*, 3(1), 2016.

[5] S. T. Bose and G. I. Park. Wall-modeled large-eddy simulation for complex turbulent flows. *Annu. Rev. Fluid Mech.*, 50:535–561, 2018.

[6] D. Lacasse, É. Turgeon, and D. Pelletier. On the judicious use of the k-ε model, wall functions and adaptivity. *Int. J. Therm. Sci.*, 43:925–938, 2004.

[7] T. Chacon Rebollo, M. Gomez Marmol, and S. Rubino. Numerical analysis of a finite element projection-based vms turbulence model with wall laws. *Computer Methods in Applied Mechanics and Engineering*, 285:379–405, 2015.

[8] A.J. Lew, G.C. Buscaglia, and P.M. Carrica. A note on the numerical treatment of the k-epsilon turbulence model. *International Journal of Computational Fluid Dynamics*, 14(3):201–209, 2001.

[9] D. Kuzmin, O. Mierka, and S. Turek. On the implementation of the k-epsilon turbulence model in incompressible flow solvers based on a finite element discretisation. *International Journal of Computing Science and Mathematics*, 1(2-4):193–206, 2007.

[10] Y. Bazilevs and T. J. R. Hughes. Weak imposition of Dirichlet boundary conditions in fluid mechanics. *Comput. Fluids*, 36:12–26, 2007.

[11] J. Nitsche. Über ein variationsprinzip zur lösung von Dirichlet-problemen bei verwendung von teilräumen, die keinen randbedingungen unterworfen sind. *Abh. Math. Semin. Univ. Hambg.*, 199:780–790, 1971.

[12] Y. Bazilevs, C. Michler, V. M. Calo, and T. J. R. Hughes. Weak Dirichlet boundary conditions for wall-bounded turbulent flows. *Comput. Methods Appl. Mech. Engrg.*, 196:4853–4862, 2007.

[13] Y. Bazilevs, C. Michler, V. M. Calo, and T. J. R. Hughes. Isogeometric variational multiscale modeling of wall-bounded turbulent flows with weakly enforced boundary conditions on unstretched meshes. *Comput. Methods Appl. Mech. Engrg.*, 36:9–15, 2010.

[14] D. B. Spalding. A single formula for the "law of the wall". *J. Appl. Mech.*, 28:455–458, 1961.

[15] B. Krank and W. A. Wall. A new approach to wall modeling in LES of incompressible flow via function enrichment. *J. Comput. Phys.*, 316:94–116, 2016.

[16] S. Kawai and J. Larsson. Wall-modeling in large eddy simulation: Length scales, grid resolution, and accuracy. *Phys. Fluids*, 24(015105), 2012.

[17] X. I. A. Yang, G. I. Park, and P. Moin. Log-layer mismatch and modeling of the fluctuating wall stress in wall-modeled large-eddy simulations. *Phys. Rev. Fluids*, 2(104601), 2017.

[18] C. C. de Wiart and S. Murman. Assessment of wall-modeled LES strategies within a Discontinuous-Galerkin spectral-element framework. *AIAA Paper*, 2017-1223.

[19] A. Frère, C. C. de Wiart, K. Hillewaert, P. Chatelain, and G. Winckelmans. Application of wall-models to Discontinuous Galerkin LES. *Phys. Fluids*, 29(085111), 2017.

[20] A. M. Vazquez, G. Houzeaux, S. Koric, A. Artigues, J. Aguado-Sierra, R. Aris, D. Mira, H. Calmet, F. Cucchietti, H. Owen, E. Casoni, A. Taha, E. D. Burness, J. M. Cela, and M. Valero. Alya: Multiphysics engineering simulation towards exascale. *J. Comput. Sci.*, 14:15–27, 2016.

[21] S. Charnyi, T. Heister, M. A. Olshankii, and L. G. Rebholz. On conservation laws of Navier-Stokes Galerkin discretizations. *J. Comput. Phys.*, 337:289–308, 2017.

[22] R. Codina. Pressure stability in fractional step finite element methods for incompressible flows. *J. Comput. Phys.*, 170:112–140, 2001.

[23] O. Lehmkuhl, G. Houzeaux, H. Owen, G. Chrysokentis, and I. Rodriguez. A low-dissipation finite element scheme for scale resolving simulations of turbulent flows. *Journal of Computational Physics*, 390:51 – 65, 2019.

[24] L. Jofre, O. Lehmkuhl, J. Ventosa, F.X. Trias, and A. Oliva. Conservation properties of unstructured finite-volume mesh schemes for the Navier-Stokes equations. *Numerical Heat Transfer, Part B: Fundamentals*, 54(1):53–79, 2014.

[25] F. Felten and T. Lund. Kinetic energy conservation issues associated with the collocated mesh scheme for incompressible flow. *Journal of Computational Physics*, 215(2):465–484, 2006.

[26] A. W. Vreman. An eddy-viscosity subgrid-scale model for turbulent shear flow: Algebraic theory and applications. *Phys. Fluids*, 16(10):3670–3681, 2004.

[27] O. Colomés, S. Badia, R. Codina, and J. Principe. Assessment of variational multiscale models for the large eddy simulation of turbulent incompressible flows. *Comput. Methods Appl. Mech. Engrg.*, 285:32–63, 2015.

[28] Y. Bazilevs, V. M. Calo, J. A. Cottrell, T. J. R. Hughes, A. Reali, and G. Scovazzi. Variational multiscale residual-based turbulence modeling for large eddy simulation of incompressible flows. *Comput. Methods Appl. Mech. Engrg.*, 197:173–201, 2007.

[29] T. J. Hughes, L. Mazzei, and K. E. Jansen. Large eddy simulation and the variational multiscale method. *Comput. Vis. Sci.*, 33:47–59, 2000.

[30] T. J. Hughes, A. A. Oberai, and L. Mazzei. Large eddy simulation of turbulent channel flows by the variational multiscale method. *Phys. Fluids*, 13(6):1784–1799, 2001.

[31] G. Houzeaux and J. Principe. A variational subgrid scale model for transient incompressible flows. *International Journal of Computational Fluid Dynamics*, 22(3):135–152, 2008.

[32] O. Lehmkuhl, G. Chrysokentis, S. Gomez, and H. Owen. Large eddy simulation for automotive aerodynamics with Alya. In *Tenth International Conference on Computational Fluid Dynamics (ICCFD10)*, Barcelona (Spain), 9-13 July 2018.

[33] O. Lehmkuhl, H. Owen, G. Chrysokentis, S. Gomez, and G. Houzeaux. On the large-eddy simulation with wall modelled support for massive separated flows at high Reynolds numbers. In *Seventh European Conference on Computational Fluid Dynamics (ECFD7)*, Glasgow (UK), 11-15 June 2018.

[34] H. Reichardt. Vollständige darstellung der turbulenten geschwindigkeits- verteilung in glatten leitungen. *ZAMM-Z. Angew. Math. Me.*, 31:208–219, 1951.

[35] C. Meneveau, C. Lunds, and W. H. Cabot. A Lagrangian dynamic subgridscale model of turbulence. *J. Fluid Mech.*, 319:353–385, 1996.

[36] S. Hoyas and J. Jiménez. Scaling of the velocity fluctuations in turbulent channels up to $Re_\tau = 2003$. *Phys. Fluids*, 18, 2006.
[37] T. Arbogast, M. F. Wheeler, and I. Yotov. Mixed finite elements for elliptic problems with tensor coefficients as cell-centered finite differences. *SIAM J. Numer. Anal.*, 34:828–852, 1997.
[38] G. I. Park. Wall-modeled large-eddy simulation of a separated flow over the NASA wall-mounted hump. *Center for Turbulence Research Annual Research Briefs*, 2015.
[39] D. Greenblatt, K. B. Paschal, C. S. Yao, J. Harris, N. W. Schaeffler, and A. E. Washburn. Experimental investigation of separation control part 1: Baseline and steady suction. *AIAA Journal*, 44(12):2820–2830, 2006.
[40] A. Kempf, M. Klein, and J. Janicka. Efficient generation of initial- and inflow-conditions for transient turbulent flows in arbitrary geometries. *Flow Turbul. Combust.*, 74:67–84, 2005.
[41] A. Avdis, S. Lardeau, and M. Leschziner. Large eddy simulation of separated flow over a two-dimensional hump with and without control by means of a synthetic slot-jet. *Flow Turb. Combust.*, 83:343–370, 2009.